

Heteroplasmon Hybridization in Stacked Complementary Plasmo-Photonic Crystals

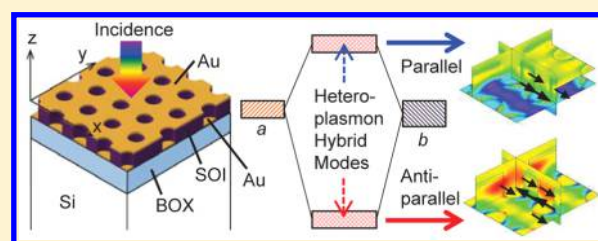
Masanobu Iwanaga* and Bongseok Choi

National Institute for Materials Science (NIMS), 1-1 Namiki, Tsukuba 305-0044, Japan

S Supporting Information

ABSTRACT: We constructed plasmo-photonic crystals in which efficient light-trapping, plasmonic resonances couple with photonic guided resonances of large density of states and high-quality factor. We have numerically and experimentally shown that heteroplasmon hybrid modes emerge in stacked complementary (SC) plasmo-photonic crystals. The resonant electromagnetic-field distributions evidence that the two hybrid modes originate from two different heteroplasmons, exhibiting a large energy splitting of 300 meV. We further revealed a series of plasmo-photonic modes in the SC crystals.

KEYWORDS: *plasmo-photonic crystals, plasmon hybridization, heteroplasmon, plasmonics, nanoimprint lithography*



Hybridization of plasmonic resonances has attracted great interest and has been investigated in various systems that include metallic nanostructures. Many hybridized systems reported so far are classified into two types: one is coupling of basically same plasmonic structures such as dimer, trimer, the higher aggregates,^{1–4} nanowire pairs,^{5–7} cut-wire pairs,^{8,9} stacked split ring resonators,^{10,11} and so on; the other type involves coupling of plasmons with other resonances such as excitons^{12–16} and a waveguide mode.¹⁷

Related to plasmon hybridization, remarkably strong anisotropic plasmons were found in stacked complementary (SC) structures.^{18–20} In these SC structures, the heteroplasmons effectively couple at a proper coupling distance. Although heteroplasmons induced in different metallic nanostructures usually have different resonant energies and couple in an inefficient manner, the SC structures realize heteroplasmons of the same resonant energy and of different resonant modes due to Babinet's principle, which states that complementary optical responses in complementary structures.²¹ Recently, other SC structures have been produced for application in fluorescence enhancement²² and coloration.²³

In spite of the many reports on plasmon hybridization, media in which plasmonic fields distribute, outside of the metallic nanostructures, have been limited to air or transparent insulators so that the photonic density of states (DOS) in the media have been sparse. However, if one incorporates large DOS media for plasmonic fields, one should be possible to access unexplored plasmon–photon hybridized systems. One of the typical large DOS media is the Si photonic crystal (PhC). By combining plasmonic crystals (PICs) that are efficiently excited by external electromagnetic (EM) waves, with PhCs of large DOS modes with high-quality(Q) factors, unique hybrid systems are expected.

In this Letter, we introduce a new class of plasmon–photonic-resonance hybridized platforms based on Si PhC slabs that we have termed *plasmo-photonic crystals*. Here, we concentrate on systematically clarifying a series of resonant modes in the SC plasmo-photonic crystals. In particular, we clarify that by making the plasmo-photonic crystals SC structures, two heteroplasmons are hybridized into two modes with a large energy splitting of 300 meV. Recently, SC crystals were shown to be a good platform for inducing significant fluorescence (FL) enhancement,²⁴ showing FL enhancement more than 100 fold for reference in a quite uniform way and suggesting that they are independent of so-called hot spots, despite current strong trend in plasmonics focusing on hot spots. The present results on resonant EM modes will provide fundamental information to explore the mechanism of the large FL enhancement and to find the optimum in the SC plasmo-photonic crystals.

As the SC structure is complex and difficult to comprehend at once, let us first explain that heteroplasmons exist in relatively simple plasmo-photonic crystals. These plasmo-photonic crystals are constituent elements that form the SC structure of interest. Figure 1a and b show schematics of plasmo-photonic crystals: the former comprises a perforated Au-film PIC on a Si PhC slab, whereas the latter consists of a Au-disk-embedded Si PhC slab. Both were set on SiO₂ substrates, the thickness of Si slab and Au along the z axis were 250 and 50 nm, respectively. The Si PhC included a hexagonal array of air holes, with a periodicity of 410 nm and air-hole diameters of 220 nm. The incident layer was air. The xyz coordinate axes were set as shown in Figure 1a and b; the x

Received: December 11, 2014

Revised: February 10, 2015

Published: February 16, 2015



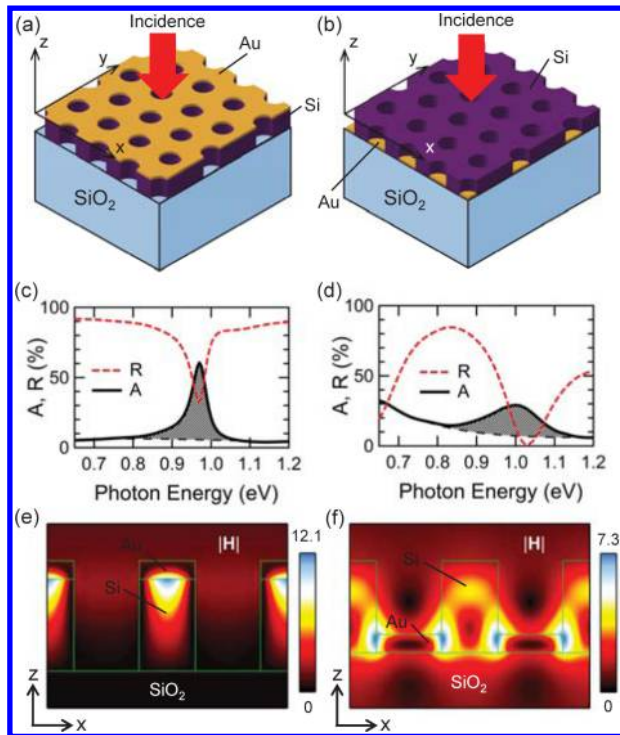


Figure 1. Heteroplasmons in plasmophotonic crystals with complementary Au structures. (a) Perforated Au-film PIC on a Si PhC slab. (b) Au-disk-array PIC in a Si PhC slab. (c) and (d) Numerically calculated absorption (A , solid line) and reflectance (R , dashed line) spectra of (a) and (b) at the normal incidence, respectively. (e) and (f) Resonant $|H|$ distributions at the A peaks in (c) and (d), respectively. The A -peak resonances in the structures (a) and (b) are labeled PlasPh modes a and b , respectively.

axes were parallel to the center-to-center direction of the nearest-neighbor air holes, and the z axes were perpendicular to the Si PhC slabs. Figure 1c and d show numerically calculated reflectance (R) and absorption (A) spectra at the normal incidence of x polarization. The linear light absorption A in the diffraction-free range was defined by

$$A = 100 - R - T \quad (1)$$

in percent, where T denotes transmittance, omitted in Figure 1. The prominent A peaks (shadow) in Figure 1c and d indicate discrete resonant modes. Note that the peaks are superimposed on continuum, which results from hot spots at the edges of the metallic nanostructures.

Figure 1e and f display absolute values of the magnetic fields $|H|$ at the A -peak energies in Figure 1c and d, respectively. The incident $|H|$ was set to 1.0. The resonant mode in Figure 1e is ascribed to the PIC-PhC interface mode, whereas that in Figure 1f is ascribed to a local-plasmon-enhanced guided mode. Evidently, the two resonant modes are hetero to each other, appearing at almost same energy. From the EM field distributions, the modes in Figure 1e and f are hybrid modes of plasmonic and photonic guided resonances; we here term the hybrid modes plasmophotonic (PlasPh) modes. Accordingly, the resonant modes in Figure 1e and f are labeled PlasPh modes a and b , respectively. As for the line width, the modes are quite broad with Q factors of 22 and 7, respectively, in Figure 1c and d. They implies that the Q factors are primarily inherited from the plasmonic resonances. From this point of view, it is possible to broadly classify the PlasPh modes into

plasmons. On the other hand, Figure 1e and f show that the resonant fields are highly localized in the Si PhC slab, implying that the large-DOS photonic guided resonances still play a role.

Related to Figure 1d, one may be interested in the lower energy range. An A peak appears at 0.645 eV, which was confirmed to come from interference in the perforated slab structure and not to be a plasmon-related mode, as shown in the Supporting Information (Figure S1). Therefore, the mode at 1.0 eV in Figure 1d is the lowest energy PlasPh mode in the plasmophotonic crystal in Figure 1b.

The numerical calculations for the R , T , and A spectra and for the EM field distributions were implemented using Fourier modal method,²⁵ often referred to as rigorously coupled-wave analysis method, incorporating the scattering matrix algorithm.²⁶ To conduct realistic computations, the permittivity of Au and Si was taken from literature collecting measured values,^{27,28} and that of air and SiO_2 was set to the representative values of 1.00057 and 2.1316, respectively.

Figure 2a shows a top-view scanning electron microscope (SEM) image (upper panel) of a SC plasmophotonic crystal with a periodicity of 410.5 nm and air holes of 220 nm diameter. A whole-view photograph (lower panel) shows a silicon-on-insulator (SOI) substrate including an SC crystal. The SC structure was formed in terms of the metal; the perforated Au film at the top layer was structurally complementary to the Au-disk array. A three-dimensional (3D) view of this SC structure is illustrated in Figure 2b. The top layer was a perforated Au PIC, the middle layer was a Si PhC slab, and the bottom layer was composed of the Au-disk-array embedded in a Si PhC slab. The SC crystals were fabricated by ultraviolet (UV) nanoimprint lithography (NIL): the nanopattern of hexagonal array by the UV NIL was introduced to the SOI layer on the buried oxide (BOX) layer, which was SiO_2 and made on a Si wafer of 625 μm thickness. Deposition of Au completed the SC crystal fabrication procedure. Further details of the procedure were previously reported.²⁴

Figure 2c shows measured R spectrum. Several R dips were observed and the lowest (or first) to sixth dips in energy are numbered 1 to 6, respectively. The incident angle θ was 5° , which is almost equivalent to the normal incidence. The plane of incidence was taken parallel to the xz plane, as shown in Figure 2b. Incidence was p -polarized, that is, the incident electric (E)-field vector E_{in} was parallel to the xz plane. In the actual sample, the Au thickness was 42 nm and the thickness of the BOX layer was 300 nm. Other structural parameters of the SC crystal were similar to those in Figure 1. We have experimentally measured many SC crystals with different structural parameters such as hole diameter, Au thickness, and SOI thickness, and found that the present set of the parameters is representative; therefore, we focus mainly on the SC crystal of the parameters specified above in order to conduct our systematic analysis of the resonant modes.

Figure 2d shows the numerically calculated R spectrum for the equivalent conditions measured in Figure 2c, presenting good agreement. The first to sixth dips were numbered similarly to those in Figure 2c. Note that the first and third modes emerge in the SC crystal, which were not observed in the constituent crystal as shown in Figure 1, and that the R spectrum of the second mode in the SC crystal is quite similar to that in Figure 1c.

To elucidate the resonant modes in the R spectra, let us examine the EM field distributions. Figure 2e to g show

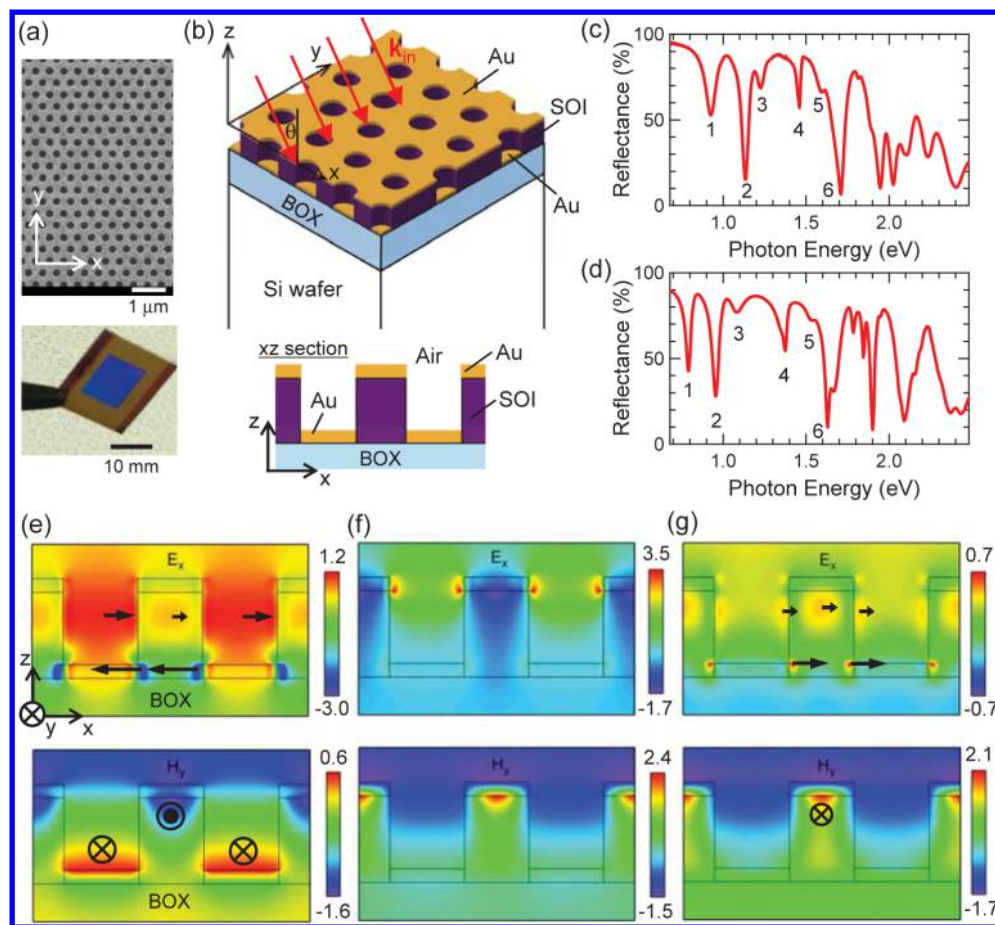


Figure 2. (a) Upper: Top-view SEM image of an SC plasmo-photonic crystal. Scale bar (white) indicates $1 \mu\text{m}$. Lower: Photograph of an SOI substrate, including a SC crystal in the central square area. Scale bar (black) indicates 10 mm . (b) Schematic of the SC plasmo-photonic crystal: a 3D view (upper) and the xz -section view (lower). (c) Measured and (d) numerically calculated R spectra at an incident angle of $\theta = 5^\circ$. (e) to (g) EM fields on the first to third resonant modes, respectively; the upper panels display snapshots of the E_x distributions, and the lower panels display the H_y distributions. Incident light came from the top along the z axis with the x polarization.

snapshots of EM fields on the first to third resonant modes, respectively, and display the xz -section view. The section was taken at the plane which includes the centers of air holes. Because the incidence was set to normal with x -polarization, the x component of the E field, E_x , and the y component of magnetic field, H_y , are shown in the upper and lower panels, respectively. The maxima of incident $|E_x|$ and $|H_y|$ were set to 1.0.

At first, Figure 2f explicitly shows the second resonant mode, which is qualitatively similar to the EM field distributions of PlasPh mode *a* in Figure 1e, though a weak signature of PlasPh *b* is simultaneously induced around the Au disk at the bottom layer. Thus, the second mode is primarily characterized as a PIC-PhC interface mode. The $|H|$ distributions of the first to sixth modes are shown in the Supporting Information (Figure S2).

On the other hand, the first and third modes in Figure 2 exhibit collectively oscillating EM fields in the whole SC structure; the EM fields have the features of both PlasPh modes *a* and *b*. Specifically, the E_x component is most enhanced around the Au disks at the bottom layer, which is a feature of PlasPh mode *b*, whereas the H_y component is most enhanced at the interface of the perforated Au PIC and Si PhC, which is a feature of PlasPh mode *a*. Therefore, it is evident that both PlasPh modes *a* and *b* contribute to the formation of the first

and third modes. As for the first mode, both E_x and H_y components contain antiparallel vectors. The set of antiparallel vectors characterizes the resonant mode; accordingly, we call the first mode *anti-parallel* mode. In contrast, locally enhanced points of the third mode have parallel vectors in the resonant EM field; we name the third mode *parallel* mode. Note again that the antiparallel and parallel modes have EM fields spreading through the whole SC structure. Qualitatively, the difference between the antiparallel and parallel modes is in the phase of their resonantly oscillating EM fields. As shown in the R spectra (Figure 2d), the antiparallel and parallel modes appear as distinct modes in energy from PlasPh modes *a* and *b*, which also supports our conclusion that the hybridization takes place in the SC structure (see Figure 3). Thus, the resonant EM field distributions evidence the hybridization of PlasPh modes *a* and *b*.

Figure 3a is an energy diagram that summarizes the first to third resonant modes in the SC crystal, based on a hybridization model of PlasPh modes *a* and *b*. At the left-hand side, the calculated A spectrum (line with gray shadow) is shown.

The hybridization model of PlasPh modes *a* and *b* is derived in a similar manner to a molecule composed of two heteroatoms of equi-energy level.²⁹ The 2×2 energy matrix is expressed as

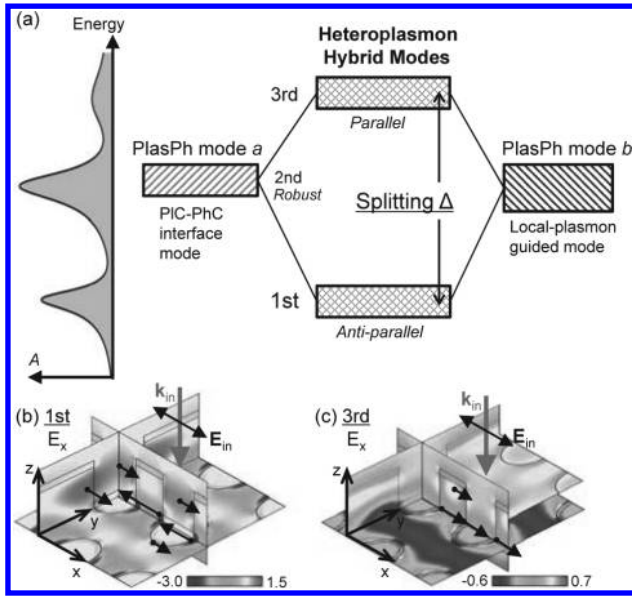


Figure 3. (a) Energy diagram based on the heteroplasmon hybridization model. Absorption A is also shown at the left. (b) and (c) 3D views of resonant E-field distributions (or the E_x components) on the first antiparallel and third parallel modes, respectively. The representative resonant points are shown with arrows.

$$\begin{pmatrix} J_{ab} - E & K_a \\ K_b & J_{ba} - E \end{pmatrix} \quad (2)$$

where J_{ab} and J_{ba} denote the exchange energy between PlasPh modes a and b , and K_a and K_b are the Coulomb energies of PlasPh modes a and b , respectively. The energy eigenvalues E_{\pm} were obtained by solving the equation such that the determinant of eq 2 is equal to 0

$$E_{\pm} = \frac{J_{ab} + J_{ba}}{2} \pm \sqrt{K_a K_b - \frac{(J_{ab} + J_{ba})^2}{4}} \quad (3)$$

Energy splitting Δ , which is defined by $\Delta = E_+ - E_-$, is written as

$$\Delta = \sqrt{4K_a K_b - (J_{ab} + J_{ba})^2} \quad (4)$$

The splitting Δ was 300 meV in the experiment (Figure 2c) and 291 meV in the numerical calculation (Figure 2d), which agree well with each other. Although it is not easy, one may think, to understand why the second mode remain to exist at almost same energy to the A peak in Figure 1c, we consider that the large energy splitting of the first and third modes allows for the second mode to exist isolatedly. Note that the second mode is highly localized at the PIC-PhC interface and similar to PlasPh mode a ; therefore, we infer that it becomes possible not to be significantly affected by a structural change from Figure 1a to Figure 2b. This uncommon behavior of the second mode was not expected in the simplified hybridization model because the simple two-level model assumes that the original heteroatoms form molecular orbitals by chemical bonding and lose their outermost states. However, in the SC plasmonic crystals, the constituent structures remain and, therefore, there is no constraint, in principle, for a mode (or modes) to exist that is (or are) similar to the original mode(s) in the large energy-splitting gap. Although these results seem to suggest that PlasPh mode a is particularly robust, we

numerically confirmed that, when incidence sheds from the substrate side, the EM field component coming from PlasPh mode b is efficiently excited. We therefore note that both PlasPh modes a and b are able to be relatively prominent in accordance with the incident configurations or k_{in} .

On the other hand, the hybridization model in eq 2 accounts for the energy levels as follows. The energies of the first and third modes are represented by E_- and E_+ , respectively. In the numerical data (Figure 2d), $E_- = 0.788$ eV and $E_+ = 1.080$ eV, so that the total exchange energy $J_{ab} + J_{ba}$ is calculated to be 1.868 eV using eq 3. In this case, the Coulomb energies K_a and K_b are almost degenerate, so we set $K = K_a \approx K_b$. From eq 4, we figure out $K \approx 0.95$ eV, which is in good agreement with the energies of the original modes, PlasPh a and b . Thus, the hybridization model self-consistently describes the energy levels.

Figure 3b and c present 3D views of the first antiparallel and third parallel modes, respectively. The snapshots of the E_x component are displayed; the xz sections are in common with Figure 2e and g. The representative resonance-enhanced fields are shown with the vectors (arrows), indicating the antiparallel and parallel enhanced fields in Figure 3b and c, respectively. We mention that nonresonant fields, which mainly appear between the air-hole array along the x axis, coexist and are particularly obvious in Figure 3c because the third mode is associated with weak light absorption and the resonant EM fields are not as intense as the first mode.

In Figure 4, we examine the change of the heteroplasmon hybrid modes for the coupling distance, that is, the thickness of

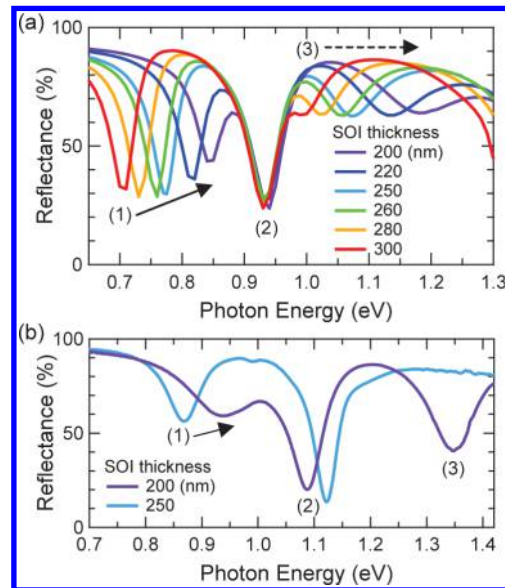


Figure 4. Coupling-distance dependence of the heteroplasmon hybrid modes, probed by varying the SOI thickness. (a) Numerically calculated R spectra at the normal incidence. (b) Measured R spectra at $\theta = 5^\circ$ under p polarization in the configuration of Figure 2b.

the SOI layer. The structural parameters were equivalent to those of the SC crystal in Figure 2, except for the SOI thickness. Figure 4a presents the R spectra at the normal incidence with x polarization, which were computed with changing the thickness from 200 to 300 nm. As the coupling distance became shorter, the first mode shifted to higher energies and became closer to the second mode. As the distance became shorter than 200 nm, the first mode finally merged with the second mode. As shown in Figure 2e, the first

mode consists of antiparallel oscillations of the resonant EM field; therefore, it is impossible to form the EM-field distributions at too short coupling distances. Thus, it is plausible for the first mode to disappear at the too short coupling distances. The third mode also shifted to higher energies as the distance became shorter. At a distance of 300 nm, the third parallel mode was located close to the second mode, whereas at 200 nm, the first mode was close to the second mode. These results suggest that both antiparallel and parallel hybrid modes appear only at a coupling-distance range that is suitable for the hybridization to occur. In contrast to the first and third modes, the second mode was almost unaffected by changes in the coupling distance; this property is consistent with the strong localization at the interface as shown in Figure 2f. Figure 4b displays measured R spectra at near normal incidence ($\theta = 5^\circ$ and p polarization) and shows that the measured results for the first to third modes are similar to the calculated results. The fabricated SC crystals had 35 nm Au thickness. A small deviation was observed in the second mode; this is probably due to small differences in the air-hole diameters in the actual samples. We experimentally confirmed using several different samples that the diameter sensitively affects the energy of the second mode.

Figure 5 shows EM-field distributions of higher n th modes ($n = 4, 5, 6$), employing the same settings to those in Figure 2e–g.

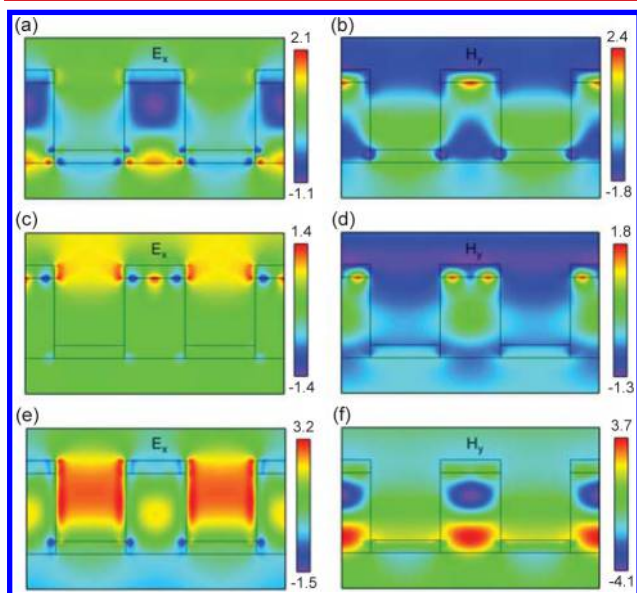


Figure 5. Resonant EM fields on the fourth to sixth resonant modes. Snapshots of the E_x and H_y components are displayed in the xz -section view, similarly to Figure 2. (a) and (b) E_x and H_y components of the fourth mode, respectively. (c) and (d) E_x and H_y of the fifth mode, respectively. (e) and (f) E_x and H_y of the sixth mode, respectively.

These are displayed in a similar way to Figure 2. The fourth mode in Figure 5a and b was attributed to a hybrid mode of the PlasPh mode a , a photonic guided mode in the Si PhC slab, and a higher local plasmon at the Au disk. The fifth mode in Figure 5c and d was found to be a second-order PIC-PhC interface mode. The sixth mode in Figure 5e and f was found to be a hybrid mode of a higher photonic guided mode and a local plasmon at the Au disk. Note that the fourth to sixth modes are not hybridized modes of PlasPh modes a and b and that the hybridization of PlasPh modes a and b is limited to the first and third modes.

We recently employed the n th mode ($n \geq 4$) in fluorescence enhancement experiments and observed up to 100-fold enhancement using the widely used rhodamine dye molecules;²⁴ we mention that the enhancement regarding the rhodamine molecules is the largest value reported to date. This study provides a systematic information on the SC crystals that are potential platforms for enhanced spectroscopy and sensing.

The plasto-photonic modes are generally characterized by dispersion in the (k_{\parallel}, ω) plane,^{17,30} where k_{\parallel} denotes wavenumbers in the xy plane of Figure 2b. The dispersion diagram in Figure 6a indicates that the first mode, numbered 1,

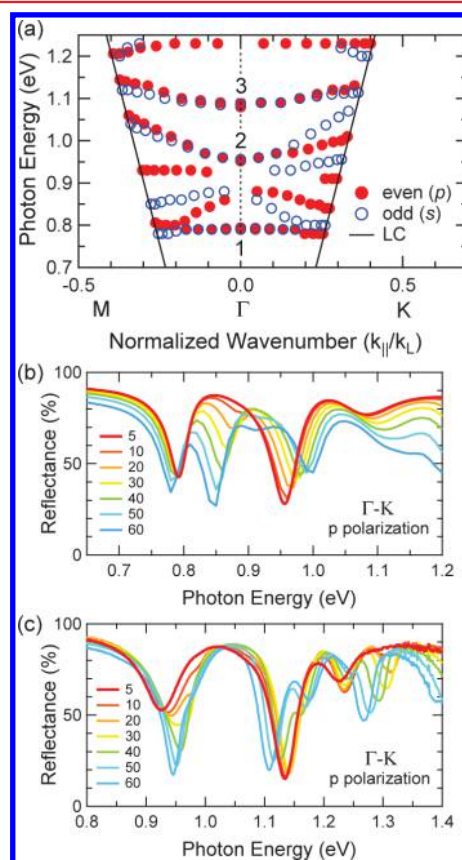


Figure 6. (a) Dispersion diagram of the plasto-photonic modes in the SC crystal. The numbers 1 to 3 indicate the first to third modes at the Γ point, respectively. Even and odd modes are shown with red closed circles and blue open circles, respectively; the former is excited at p polarization and the latter at s polarization. Light cone (LC) in air is shown with oblique lines. (b) and (c) Calculated and measured R spectra dependent on incident angles from 5° to 60° , respectively. The incidence was p -polarized and the in-plane wavevector k_{\parallel} was along the Γ - K direction.

at the Γ point is nearly local or almost independent of k_{\parallel} and that the second and third modes are quadratically dependent on wavenumbers, taking a concave profile in the $(k_{\parallel}/k_L, \hbar\omega)$ plane where k_L is the lattice wavenumber, equal to $2\pi/d$ (d = the periodicity). The first to third modes have two-dimensional symmetry in group theory³¹ around the Γ point, that is, degenerate modes of even and odd parity. The definitions of parity and polarizations are consistent with those defined for the photonic band diagram in the Supporting Information (Figure S3). At the Γ point, large energy splitting Δ in eq 4 is observed between the first and third modes. The gap Δ increases by small amounts as $|k_{\parallel}|$ increases. One may expect

so-called anticrossing behavior concerning the hybridized modes; however, the present SC system is not the simple polariton–polariton coupling system in previous reports.^{14,16,17} Instead, in the large energy splitting, several $k_{||}$ - and parity-dependent asymmetric modes, which stem from the photonic guided modes, exist in addition to the second mode. Therefore, there is no reason, in principle, to expect anticrossing behavior in the SC system. Actually, the dispersions of the first and third modes are quite similar to some of the dispersions in strong light–electronic-state coupling systems.^{13,32} The dispersions were extracted from the computed A peaks obtained from eq 1. Incidence was set to come from air; therefore, the dispersions in Figure 6a were limited inside the light cone (LC), as shown with oblique lines. Figure 6b presents a series of calculated R spectra contributing to the dispersion in Figure 6a. Figure 6c shows the measured R spectra, which corresponds to the spectra in Figure 6b. Although some modes at deeply oblique angles appear in different ways, the asymmetric modes were also observed in the experiment.

Let us consider the contribution from the underlying Si PhC slab. In the Si PhC slab without any Au nanostructure, the photonic guided resonances with large DOS and high-Q factor are the most prominent feature though there is no full photonic bandgap.³³ The photonic band diagram of the Si PhC slab and the DOS spectrum at the Γ point are shown in the Supporting Information (Figure S3). The lowest large-DOS guided mode at the Γ point exists at approximately 1.1 eV; this energy is close to those of PlasPh modes a and b , indicating that the lowest large-DOS photonic guided mode contributes to the hybrid plasmophotonic modes. As mentioned in Figure 1, the photonic guided mode plays a role, in the plasmophotonic structures, to selectively localize the resonant EM fields in the Si PhC slab. If the Si PhC slab is replaced with Si slab without air holes, EM fields spread inside the slab and hybridized modes like the first and third modes in Figure 2 do not appear, as shown in the Supporting Information (Figure S4).

As mentioned previously, plasmon–photon hybridization was investigated using low DOS media for plasmonic fields in almost all the cases.^{1–11} The only exception was done by using whispering-gallery microcavity³⁴ though it was not a periodic structure; a high-Q-factor whispering-gallery resonance was coupled with interface plasmon, and the resultant mode had a quite high-Q factor, being close to 3000, which is primarily interpreted as a kind of whispering-gallery mode and has weak coupling to the external EM fields in comparison with the present SC plasmophotonic crystals.

In conclusion, we have clarified heteroplasmons (PlasPh modes a and b) in the plasmophotonic crystals and fabricated the SC plasmophotonic crystals for the hybridization. Consequently, we revealed that the first and third resonant modes manifest as heteroplasmon hybridization, exhibiting significant energy splitting up to 300 meV. It was also revealed that the second mode, which is a hybrid mode of the lowest large-DOS photonic guided resonance and interface plasmonic resonance at the PIC-PhC boundary, is a highly localized mode and exists in the large energy-splitting gap between the first and third modes. In addition, other higher modes from the fourth to sixth were shown to be higher hybrid modes resulting from the coupling of higher plasmonic modes in the PICs with photonic guided resonances in Si PhC slab. These systematic clarifications of the EM resonant modes will be a firm basis for applications of the SC plasmophotonic crystals such as fluorescence sensing.²⁴

■ ASSOCIATED CONTENT

Supporting Information

We provide EM-field distributions of other plasmophotonic crystals for comparison with the SC plasmophotonic crystal, a series of |H| distributions in the SC crystal, and DOS spectrum and photonic band diagram of a Si PhC slab underlying the SC crystal. This material is available free of charge via the Internet at <http://pubs.acs.org/>.

■ AUTHOR INFORMATION

Corresponding Author

*E-mail: iwanaga.masanobu@nims.go.jp.

Notes

The authors declare no competing financial interest.

■ ACKNOWLEDGMENTS

We deeply thank Dr. Tetsuyuki Ochiai (NIMS) for the photonic-band calculations and useful suggestions to the manuscript. This study was partially supported by a Grant-in-Aid (number 22109007) from the Ministry of Education, Culture, Sport, Science and Technology, Japan. M.I. also acknowledges the support for numerical implementations at Cyberscience Center, Tohoku University and Cybermedia Center, Osaka University through HPCI System Research Project (ID: hp120066, hp140068), and financial support by a Grant-in-Aid (number 26706020) from Japan Society for the Promotion of Science. Nanofabrications and the characterizations were conducted at NanoIntegration Foundry, Low-Carbon Research Network, and MANA Foundry in NIMS.

■ REFERENCES

- (1) Prodan, E.; Radloff, C.; Halas, N. J.; Nordlander, P. *Science* **2003**, *302*, 419–422.
- (2) Brandl, D. W.; Mirin, N. A.; Nordlander, P. *J. Phys. Chem. B* **2006**, *110*, 12302–12310.
- (3) Fan, J. A.; Wu, C.; Bao, K.; Bao, J.; Bardhan, R.; Halas, N. J.; Manoharan, V. N.; Nordlander, P.; Shvets, G.; Capasso, F. *Science* **2010**, *328*, 1135–1138.
- (4) Hentschel, M.; Saliba, M.; Vogelgesang, R.; Giessen, H.; Alivisatos, A. P.; Liu, N. *Nano Lett.* **2010**, *10*, 2721–2726.
- (5) Christ, A.; Ekinci, Y.; Solak, H. H.; Gippius, N. A.; Tikhodeev, S. G.; Martin, O. J. F. *Phys. Rev. B* **2007**, *76*, 201405(R).
- (6) Christ, A.; Martin, O. J. F.; Ekinci, Y.; Gippius, N. A.; Tikhodeev, S. G. *Nano Lett.* **2008**, *8*, 2171–2175.
- (7) Taubert, R.; Ameling, R.; Weiss, T.; Christ, A.; Giessen, H. *Nano Lett.* **2011**, *11*, 4421–4424.
- (8) Liu, N.; Guo, H.; Fu, L.; Kaiser, S.; Schweizer, H.; Giessen, H. *Adv. Mater.* **2007**, *19*, 3628–3632.
- (9) Ameling, R.; Giessen, H. *Nano Lett.* **2010**, *10*, 4394–4398.
- (10) Liu, H.; Genov, D. A.; Wu, D. M.; Liu, Y. M.; Liu, Z. W.; Sun, C.; Zhu, S. N.; Zhang, X. *Phys. Rev. B* **2007**, *76*, 073101.
- (11) Liu, N.; Liu, H.; Zhu, S.; Giessen, H. *Nat. Photonics* **2009**, *3*, 157–162.
- (12) Pockrand, I.; Brillante, A.; Möbius, D. *J. Chem. Phys.* **1982**, *77*, 6289–6295.
- (13) Hobson, P. A.; Barnes, W. L.; Lidzey, D. G.; Gehring, G. A.; Whittaker, D. M.; Skolnick, M. S.; Walker, S. *Appl. Phys. Lett.* **2002**, *81*, 3519–3521.
- (14) Hakala, T. K.; Toppari, J. J.; Kuzyk, A.; Pettersson, M.; Tikkanen, H.; Kunttu, H.; Törmä, P. *Phys. Rev. Lett.* **2009**, *103*, 053602.
- (15) Hutchison, J. A.; Schwartz, T.; Genet, C.; Devaux, E.; Ebbesen, T. W. *Angew. Chem., Int. Ed.* **2012**, *51*, 1592–1596.

- (16) Väkeväinen, A. I.; Moerland, R. J.; Rekola, H. T.; Eskelinen, A.-P.; Martikainen, J.-P.; Kim, D.-H.; Törmä, P. *Nano Lett.* **2014**, *14*, 1721–1727.
- (17) Christ, A.; Tikhodeev, S. G.; Gippius, N. A.; Kuhl, J.; Giessen, H. *Phys. Rev. Lett.* **2003**, *91*, 183901.
- (18) Iwanaga, M. *Appl. Phys. Lett.* **2010**, *96*, 083106.
- (19) Iwanaga, M. *Opt. Express* **2010**, *18*, 15389–15398.
- (20) Iwanaga, M. *Phys. Rev. B* **2010**, *82*, 155402.
- (21) Born, M.; Wolf, E. *Principles of Optics*, 7th ed.; Cambridge Univ. Press: Cambridge, 1999; Chapter 11.
- (22) Zhang, W.; Ding, F.; Li, W.-D.; Wang, Y.; Hu, J.; Chou, S. Y. *Nanotechnology* **2012**, *23*, 225301.
- (23) Clausen, J. S.; Højlund-Nielsen, E.; Christiansen, A. B.; Yazdi, S.; Grajower, M.; Taha, H.; Levy, U.; Kristensen, A.; Mortensen, N. A. *Nano Lett.* **2014**, *14*, 4499–4504.
- (24) Choi, B.; Iwanaga, M.; Miyazaki, H. T.; Sakoda, K.; Sugimoto, Y. *J. Micro/Nanolith., MEMS, MOEMS* **2014**, *13*, 023007.
- (25) Li, L. *J. Opt. Soc. Am. A* **1997**, *14*, 2758–2767.
- (26) Li, L. *J. Opt. Soc. Am. A* **1996**, *13*, 1024–1035.
- (27) Rakić, A. D.; Djurušić, A. B.; Elazar, J. M.; Majewski, M. L. *Appl. Opt.* **1998**, *37*, 5271–5283.
- (28) Palik, E. D. *Handbook of Optical Constants of Solids II*; Academic: San Diego, 1991.
- (29) For example, Feynman, R. P.; Leighton, R. B.; Sands, M. *The Feynman Lectures on Physics*, Vol. 3; Addison-Wesley: Boston, MA, 1971.
- (30) Iwanaga, M. *Sci. Technol. Adv. Mater.* **2012**, *13*, 053002.
- (31) Sakoda, K. *Optical Properties of Photonic Crystals*, 2nd ed.; Springer: Berlin, 2005.
- (32) Schwartz, T.; Hutchison, J. A.; Léonard, J.; Genet, C.; Haacke, S.; Ebbesen, T. W. *ChemPhysChem* **2013**, *14*, 125–131.
- (33) Ochiai, T.; Sakoda, K. *Phys. Rev. B* **2001**, *63*, 125107.
- (34) Min, B.; Ostby, E.; Sorger, V.; Ulin-Avila, E.; Yang, L.; Zhang, X.; Vahala, K. *Nature* **2009**, *457*, 455–458.